

Article

# Coupling LaNiO<sub>3</sub> Nanorods with FeOOH Nanosheets for Oxygen Evolution Reaction

Minghong Sun <sup>1</sup>, Qicheng Zhang <sup>1</sup>, Qiming Chen <sup>1</sup>, Xiaohan Hou <sup>1</sup>, Wenchao Peng <sup>1</sup> , Yang Li <sup>1</sup> , Fengbao Zhang <sup>1</sup>, Qing Xia <sup>1</sup> and Xiaobin Fan <sup>1,2,3,\*</sup>

<sup>1</sup> State Key Laboratory of Chemical Engineering, School of Chemical Engineering and Technology, Tianjin University, Tianjin 300072, China; minghongsun@tju.edu.cn (M.S.); zhangqicheng@tju.edu.cn (Q.Z.); qimingchen@tju.edu.cn (Q.C.); xiaohanhou@tju.edu.cn (X.H.); wenchao.peng@tju.edu.cn (W.P.); liyang1895@tju.edu.cn (Y.L.); fbxzhang@tju.edu.cn (F.Z.); xiaqing@tju.edu.cn (Q.X.)

<sup>2</sup> Haihe Laboratory of Sustainable Chemical Transformations, Tianjin 300192, China

<sup>3</sup> Institute of Shaoxing, Tianjin University, Shaoxing 312300, China

\* Correspondence: xiaobinfan@tju.edu.cn

**Abstract:** Perovskite-based electrocatalysts with compositional flexibility and tunable electronic structures have emerged as one of the promising non-noble metal candidates for oxygen evolution reaction (OER). Here, we propose a heterostructure comprising perovskite oxide (LaNiO<sub>3</sub>) nanorods and iron oxide hydroxide (FeOOH) nanosheets as an effective electrochemical catalyst for OER. The optimized 0.25Fe-LNO catalyst with an interesting 1D-2D hierarchical structure shows a low overpotential of 284 mV at 10 mA cm<sup>-2</sup> and a small Tafel slope of 69 mV dec<sup>-1</sup>. The enhanced performance can be explained by the synergistic effect between LaNiO<sub>3</sub> and FeOOH, resulting in an improved electrochemically active surface area, facilitated charge transfer and the optimized adsorption of OH intermediates.



**Citation:** Sun, M.; Zhang, Q.; Chen, Q.; Hou, X.; Peng, W.; Li, Y.; Zhang, F.; Xia, Q.; Fan, X. Coupling LaNiO<sub>3</sub> Nanorods with FeOOH Nanosheets for Oxygen Evolution Reaction. *Catalysts* **2022**, *12*, 594. <https://doi.org/10.3390/catal12060594>

Academic Editors: Yongjun Feng, Zhenghua Tang, Marc Cretin and Sophie Tingry

Received: 10 April 2022

Accepted: 24 May 2022

Published: 30 May 2022

**Publisher's Note:** MDPI stays neutral with regard to jurisdictional claims in published maps and institutional affiliations.



**Copyright:** © 2022 by the authors. Licensee MDPI, Basel, Switzerland. This article is an open access article distributed under the terms and conditions of the Creative Commons Attribution (CC BY) license (<https://creativecommons.org/licenses/by/4.0/>).

**Keywords:** perovskite oxide; oxygen evolution; FeOOH; electrocatalyst

## 1. Introduction

Faced with the growing energy crisis and environmental issues, it is imperative to exploit effective and green devices for energy storage and conversion [1–3]. The rational design of oxygen evolution reaction (OER) electrocatalysts is of great significance to the applications of water electrolyzers [4,5]. However, the sluggish kinetics and high overpotential of OER caused by the complex multiple electron transfer process are obstacles to its large-scale application [6]. Although Ir- and Ru-based oxide are recognized as the benchmark OER catalysts with high electrochemical activity, their high cost and low abundance have compelled the development of earth-abundant and efficient non-noble metal OER catalysts [7,8]. In recent years, tremendous efforts have been devoted to research on transition metal-based catalysts, such as transition metal oxides, [9] sulfides [10] and oxyhydroxides [11].

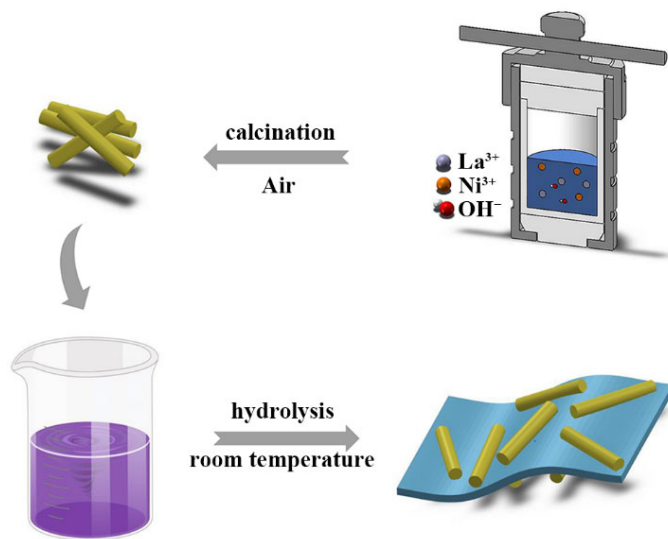
As the promising candidates, perovskite oxides with a general formula of ABO<sub>3</sub> have attracted increasing attention owing to their compositional flexibility, tunable electronic structures and chemical stability [12,13]. To guide the design of ABO<sub>3</sub> catalysts for OER,  $(\Delta G_{O^*} - \Delta G_{OH^*})$  [14] and e<sub>g</sub> orbital filling [15] have been proposed as catalytic activity descriptors. According to the volcano maps obtained by describing OER activity with the descriptors, LaNiO<sub>3</sub> (LNO) shows better performance in the family of ABO<sub>3</sub> and is considered a prospective candidate for optimization [14–16]. Nonetheless, the electrocatalytic performance of the LNO remains unsatisfactory due to its limited active sites and poor electrical conductivity [13,17]. On the one hand, the perovskite oxides synthesized by traditional solid-state and sol-gel methods generally have a large size and low surface area, resulting in poor catalytic activity. Previous studies have demonstrated that morphology

engineering is an effective method to enhance the activity of perovskite-based electrocatalysts by increasing the surface area, such as nanorods [18], nanofibers [19] nanotubes [20] and porous structure [21]. On the other hand, intrinsic catalytic activity is also an important consideration in perovskite-based catalyst design [22]. The adsorption and desorption of OH are key steps in the alkaline OER process, and optimizing the adsorption energy of intermediates can boost OER intrinsic catalytic activity [23,24]. Constructing heterogeneous structures is a general method which can not only modulate the electronic structure but also generate synergistically active sites [13,19,25]. Among the various perovskite-based composites, perovskite/transition metal-based composites exhibit excellent performance, such as  $\text{CoS}_2/\text{LaCo}_{0.2}\text{Fe}_{0.8}\text{O}_3$ , [12]  $\text{MoSe}_2/\text{La}_{0.5}\text{Sr}_{0.5}\text{CoO}_{3-\delta}$  [26] and  $\text{Fe}_2\text{O}_3/\text{LaNiO}_3$  [27]. Meanwhile, FeOOH is considered a promising catalyst for OER, with high OH adsorption capacity [28,29] that can be introduced into perovskite-based composites to accelerate OER kinetics.

Here, we propose the 1D-2D  $\text{LaNiO}_3$  nanorods-FeOOH nanosheets heterostructure as an effective catalyst for oxygen evolution reaction. The optimized 0.25Fe-LNO catalyst displays a lower overpotential and a smaller Tafel slope when compared with the other counterparts. The experimental results demonstrate that the excellent OER catalytic performance of  $\text{LaNiO}_3/\text{FeOOH}$  could be attributed to the synergistic effect between LNO and FeOOH as well as the morphology engineering of LNO, encouraging the strong electron interaction, the facilitated charge transfer and the improved active sites.

## 2. Results and Discussion

Scheme 1 schematically illustrates the synthesis process for hierarchical  $\text{LaNiO}_3/\text{FeOOH}$  composites by two steps. Briefly, the perovskite LNO nanorods were synthesized by the hydrothermal method and then immersed in alkaline solutions of  $\text{K}_2\text{FeO}_4$  with different concentrations to obtain the hierarchical LNO-FeOOH composites, denoted as  $x\text{Fe-LNO}$ ,  $x = 0.125, 0.25, 0.5, 0.75$ . The more experimental details are shown in the experimental section.



**Scheme 1.** Schematic illustration for the synthesis of Fe-LNO.

The powder X-ray diffraction (XRD) patterns of LNO, FeOOH and  $x\text{Fe-LNO}$  are shown in Figure 1a. The diffraction peaks of the obtained LNO match well with the standard peaks of  $\text{LaNiO}_3$  (JCPDS No. 33-0711), whereas FeOOH shows no diffraction peak. Generally, FeOOH prepared by hydrolysis at low temperatures has poor crystallinity without obvious diffraction peaks in the XRD spectrum [30–32]. Although the diffraction peaks of FeOOH appear in some cases, the peak intensity is also very weak due to the room temperature synthesis [33]. In addition, experimental conditions such as concentration and whether or not to stir could also affect the crystallinity. According to the XRD spectrum, the

FeOOH prepared in this work has a lower crystallinity and presents an amorphous form. It is worth noting that the diffraction peaks' position corresponding to LaNiO<sub>3</sub> (JCPDS No. 33-0711) remains unchanged in the xFe-LNO samples, but the corresponding peak intensity gradually decreases with the increase in x value. This phenomenon is inconsistent with Fe doping, which will cause a shift in the diffraction peaks corresponding to LaNiO<sub>3</sub> to lower angles in the XRD spectrum [34,35], but it is consistent with the formation of amorphous substances on the surface of LNO [20]. Furthermore, new diffraction peaks corresponding to La(OH)<sub>3</sub> (JCPDS No. 36-1481) appear, owing to the presence of NaOH in the K<sub>2</sub>FeO<sub>4</sub> solution, but the perovskite structure remains. To identify the FeOOH phase, Raman spectra were performed (Figure 1b). For the hydrolysis products of K<sub>2</sub>FeO<sub>4</sub>, the six characteristic peaks (214, 283, 310, 377, 517 and 674 cm<sup>-1</sup>) are well-indexed to the layered γ-FeOOH structure. The peak at 377 cm<sup>-1</sup> is the characteristic of γ-FeOOH, and the peaks at 310 and 517 cm<sup>-1</sup> are ascribed to the Fe–OH stretching modes. The broad peak located at 674 cm<sup>-1</sup> can be attributed to the stretching of Fe–O, [33,36,37] while the weak peak at 1310 cm<sup>-1</sup> corresponds to the H<sub>2</sub>O intercalated in the layered FeOOH [37–39]. Note that the LNO sample has no vibrational modes of Raman response, and the 0.25Fe-LNO exhibits weaker vibrational bands at 310, 377, 517 and 674 cm<sup>-1</sup> compared with the LNO nanorods counterpart. The peaks at 214 cm<sup>-1</sup> and 283 cm<sup>-1</sup> correspond to the layer structure, which mainly depends on the degree of disorder (stacking fault) and/or grain size [40]. The disappearance of the peaks only indicates that the LNO stacking on the FeOOH surface weakens the mode of the layer structure. These results suggest the successful formation of the FeOOH-LNO composite.

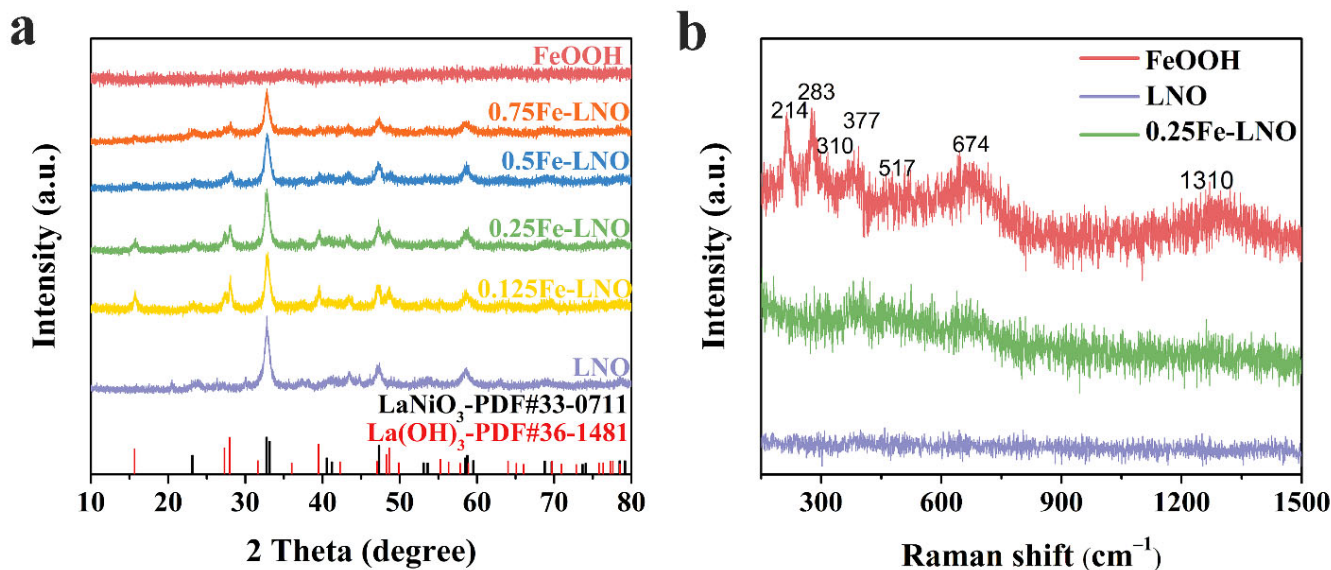


**Figure 1.** (a) XRD pattern of LNO, FeOOH and Fe-LNO samples (b) Raman spectrum of LNO, FeOOH and 0.25Fe-LNO.

Scanning electron microscopy (SEM) reveals that the hydrothermal synthesized LNO exhibits a nanorod structure with lengths of 30–100 nm and diameters of 10–20 nm (Figure 2a), while the FeOOH, as the hydrolysates of K<sub>2</sub>FeO<sub>4</sub>, is composed of aggregated nanosheets (Figure S1, Supplementary Materials). The drying process in the preparation leads to agglomeration, which makes the SEM image of 0.25Fe-LNO unable to fully display the morphology of the sample. Nonetheless, the nanosheets can still be identified in the marked regions of Figure 2b, demonstrating the successful introduction of FeOOH and forming the composites. Note that this hierarchical structure results in an increase in the specific surface area (SSA). The Brunauer–Emmett–Teller (BET) analysis actually shows that the SSA of the obtained 0.25Fe-LNO is 40.4 m<sup>2</sup> g<sup>-1</sup>, which is almost twice that of the LNO nanorods (22.8 m<sup>2</sup> g<sup>-1</sup>) (Figure S2, Supplementary Materials). Transmission

electron microscopy (TEM) was carried out to further unveil the morphology and structure of LNO and 0.25Fe-LNO. TEM images at different magnifications of 0.25Fe-LNO (Figures 2d and S3, Supplementary Materials) demonstrate that the morphology of the LNO nanorods with the diameters of 10–20 nm remained basically unchanged, which is consistent with the SEM and TEM image of the LNO (Figure 2a,c). More importantly, it can be clearly seen that the nanorods attach randomly to the thin nanosheets, indicating the existence of 1D-2D heterostructures that are consistent with the synthesis results of Scheme 1. The composition of this heterostructure was further determined by the high-resolution TEM (HRTEM) images. The lattice fringes of the LNO nanorods are measured to be 0.273 and 0.384 nm, corresponding to the (110) and (101) facets of  $\text{LaNiO}_3$  (JCPDS No. 33-0711), respectively (Figure S4, Supplementary Materials). As shown in Figure 2e,f, the HRTEM images of 0.25Fe-LNO reflects the intact contact between the LNO nanorods and the FeOOH nanosheets, and the FeOOH has no regular interplanar spacing due to poor crystallinity, which is consistent with the results of the XRD. To further identify the composition of the nanosheets, the HAADF-TEM image of 0.25Fe-LNO and the corresponding elemental mapping images are shown in Figure S5 (Supplementary Materials), which can further prove the existence of FeOOH nanosheets and the formation of a 1D-2D  $\text{LaNiO}_3$  nanorods-FeOOH nanosheets heterostructure. The clear and coherent interface between the LNO and FeOOH displayed in the TEM image of 0.25Fe-LNO can favor the electronic transfer and the biphasic synergy catalysis, as verified by subsequent X-ray photoelectron spectroscopy (XPS) and electrochemical measurements [19].

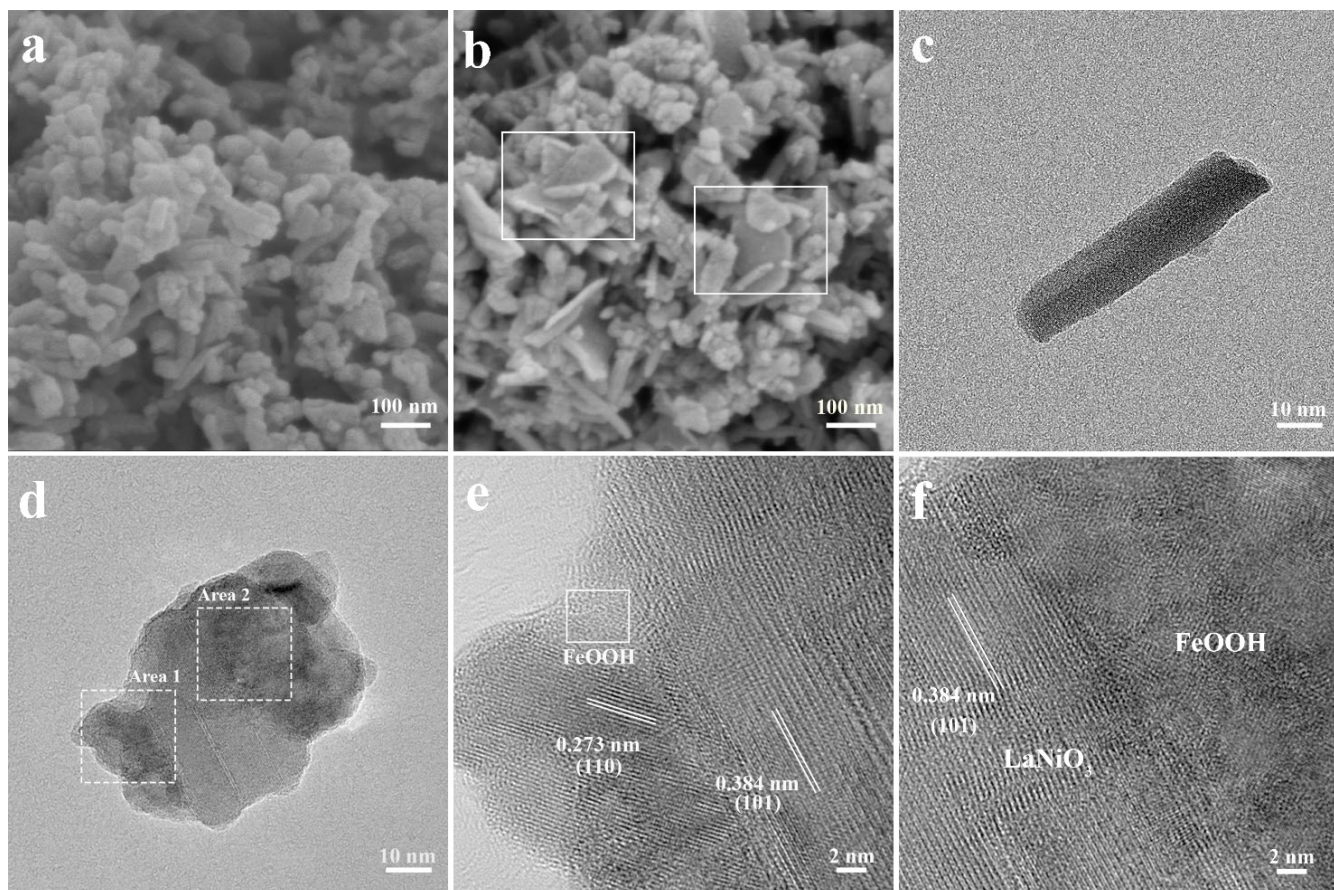


**Figure 2.** SEM images of (a) LNO and (b) 0.25Fe-LNO. TEM images of (c) LNO and (d) 0.25Fe-LNO. HRTEM image of 0.25Fe-LNO corresponding to the (e) Area 1 and (f) Area 2, as marked in (d).

The elemental compositions and electronic structure of the LNO, FeOOH and 0.25Fe-LNO were investigated by XPS. The survey spectra (Figure S6, Supplementary Materials) confirm that La, Ni, Fe and O are the main elements in the 0.25Fe-LNO. The XPS spectra of the La 3d

and Ni 2p of LNO and 0.25Fe-LNO are shown in Figure 3a,b. Considering that the binding energy region of La 3d<sub>3/2</sub> and Ni 2p<sub>3/2</sub> partially overlap, [41,42] the peak position and intensity of La 3d<sub>3/2</sub> and Ni 2p<sub>3/2</sub> are distinguished by those of La 3d<sub>5/2</sub> and Ni 2p<sub>1/2</sub> [43]. Moreover, it is noted that the peaks of La 3d<sub>3/2</sub> and 3d<sub>5/2</sub> are multiplet-split owing to the charge transfer from the bonded oxygen to the empty La 4f [44]. The La 3d<sub>5/2</sub> and 3d<sub>3/2</sub> of LNO are located at 834.37/837.80 and 850.79/853.43, whereas those of 0.25Fe-LNO are positioned at 834.87/838.35 and 851.34/853.98, respectively. It demonstrates a binding energy upshift of 0.55 eV in the 0.25Fe-LNO compared to the LNO nanorods [44,45]. Similarly, the Ni 2p spectra of 0.25Fe-LNO consist of Ni 2p<sub>3/2</sub> (855.65 eV) and Ni 2p<sub>1/2</sub> (872.95 eV), with two satellites whose binding energy is 0.20 eV higher than those of LNO, implying an increased oxidation state of Ni [46]. These shifts in the peak positions indicate a shift in the Fermi level with respect to the core levels rather than the charging effects. First, the charge compensation and energy calibration were used to remove the charge effect. Further, the charging effect caused by a significant net positive charge accumulates at the surface of insulators and will lead to a positive shift in the binding energy of the sample. Given that the conductivity of LNO is worse than that of 0.25Fe-LNO, the charging effect of LNO should be more obvious than that of 0.25Fe-LNO. However, the binding energy of 0.25Fe-LNO is positively shifted compared to that of LNO in the Ni 2p and La 3d XPS spectrum. High-spin Fe<sup>3+</sup> and Fe<sup>2+</sup> cause complex multiplet-split in the Fe 2p spectrum [47]. Since the multiple splitting of Fe<sup>2+</sup> and Fe<sup>3+</sup> is too complicated to distinguish, and dividing Fe 2p into different oxidation states could also identify the shift in the peak positions well, it is not necessary to distinguish multiple peaks for each oxidation state [33,48]. As demonstrated in Figure 3c, the Fe 2p spectra consist of two spin-orbit doublets with satellites, and the Fe species could be deconvoluted into Fe<sup>2+</sup> and Fe<sup>3+</sup>. The peaks of 0.25Fe-LNO at 712.16/725.42 and 710.19/723.45 eV correspond to Fe<sup>3+</sup> 2p<sub>3/2</sub>/2p<sub>1/2</sub> and Fe<sup>2+</sup> 2p<sub>3/2</sub>/2p<sub>1/2</sub>, respectively [49]. Further, the peak at around 706 eV is assigned to the Ni Auger peak in the 0.25Fe-LNO. Compared with those of pure FeOOH, the Fe 2p peaks of 0.25Fe-LNO downshift 0.29 eV. The chemical shifts strongly confirm the electron transfer from the LNO nanorods to the FeOOH in 0.25Fe-LNO, which can lead to a synergistic effect to improve the OER electrocatalytic activity. [50] In addition, Figure 3d displays the O 1 s spectra of LNO and 0.25Fe-LNO, which can be deconvoluted into four peaks corresponding to the lattice oxygen species (O<sup>2-</sup>, 528.32 eV), superoxidative oxygen (O<sub>2</sub><sup>2-</sup>/O<sup>-</sup>, 529.44 eV), hydroxyl groups (-OH, 531.12 eV) and adsorbed water (H<sub>2</sub>O, 532.18 eV) [51]. The content of adsorbed water oxygen mainly depends on the atmospheric conditions rather than the material properties [48]. When calculating the proportion of oxygen species, the content of adsorbed water should be removed. It is noted that the proportion of hydroxyl groups in the oxygen species of 0.25Fe-LNO (76.3%) is significantly higher than that of LNO (62.5%), indicating the higher surface coverage ( $\theta$ ) of the OH species in the 0.25Fe-LNO sample [52]. A high  $\theta$  value is beneficial for OH adsorption on the catalyst surface, which can enhance OER intrinsic activity [26,52].

The OER catalytic performance of as-prepared catalysts was measured in a 1 M KOH electrolyte. As shown in Figure 4a, the linear sweep voltammetry (LSV) polarization curves demonstrate that the OER activity of the xFe-LNO catalysts significantly exceeds that of the LNO or FeOOH alone. Among them, the 0.25Fe-LNO catalyst displays the best performance, with the lowest overpotential of 284 mV at the current density of 10 mA cm<sup>-2</sup>—even better than commercial RuO<sub>2</sub> and IrO<sub>2</sub> (Figure S7, Supplementary Materials). The LNO and FeOOH exhibit poor performance, with overpotentials of 363 and 330 mV, generating the same density current of 10 mA cm<sup>-2</sup>, respectively. The Tafel slopes of xFe-LNO, FeOOH and LNO are shown in Figure 4b, which are used to reflect the OER kinetics reaction rate and the charge transfer ability [7,53]. As expected, the 0.25Fe-LNO sample displays the lowest Tafel slope of 69 mV·dec<sup>-1</sup>, which is significantly smaller than those of the LNO nanorods (120 mV·dec<sup>-1</sup>), FeOOH nanosheets (92 mV·dec<sup>-1</sup>) and RuO<sub>2</sub> (84 mV·dec<sup>-1</sup>). Note that all the Tafel slopes of the other xFe-LNOs catalysts are smaller than those of the individual components. For the four-electron transfer oxygen

evolution reaction, the Tafel slope is closely related to the reaction mechanism and can even predict the rate-determining step. Furthermore, the rate-determining step moves closer to the beginning part of the multiple-electron transfer reaction as the Tafel slope increases. As the first electron transfer reaction, when the adsorption of the OH groups is the rate-determining step, the corresponding Tafel slope is  $120 \text{ mV dec}^{-1}$  [54]. This suggests that the adsorption of OH groups is the OER rate-limiting step of LNO. These low Tafel slopes of the xFe-LNO could be attributed to the high coverage of the hydroxyl group and the obvious charge transfer between FeOOH and LNO, as discussed above. During the electrochemical test of perovskite-based catalysts, conductive agents are usually added to the ink in a certain mass ratio to remove the electrode conductivity limit. To further demonstrate the catalyst-specific results, the LSV polarization curves and corresponding Tafel plots of these samples without Ketjenblack carbon were added in the Supplementary Materials (Figure S8). The catalyst-specific activity of 0.25Fe-LNO significantly surpasses that of LNO and FeOOH. The addition of Ketjenblack carbon can improve the performance of these catalysts to varying degrees, and the positive influence on LNO and FeOOH is greater than that on 0.25Fe-LNO, indicating that the heterostructure enhances the conductivity of LNO and FeOOH. The resistivities of 0.25Fe-LNO are almost twice those of LNO, as tested by a four-probe resistance tester, which further confirmed the above conclusion (Supplementary Materials).

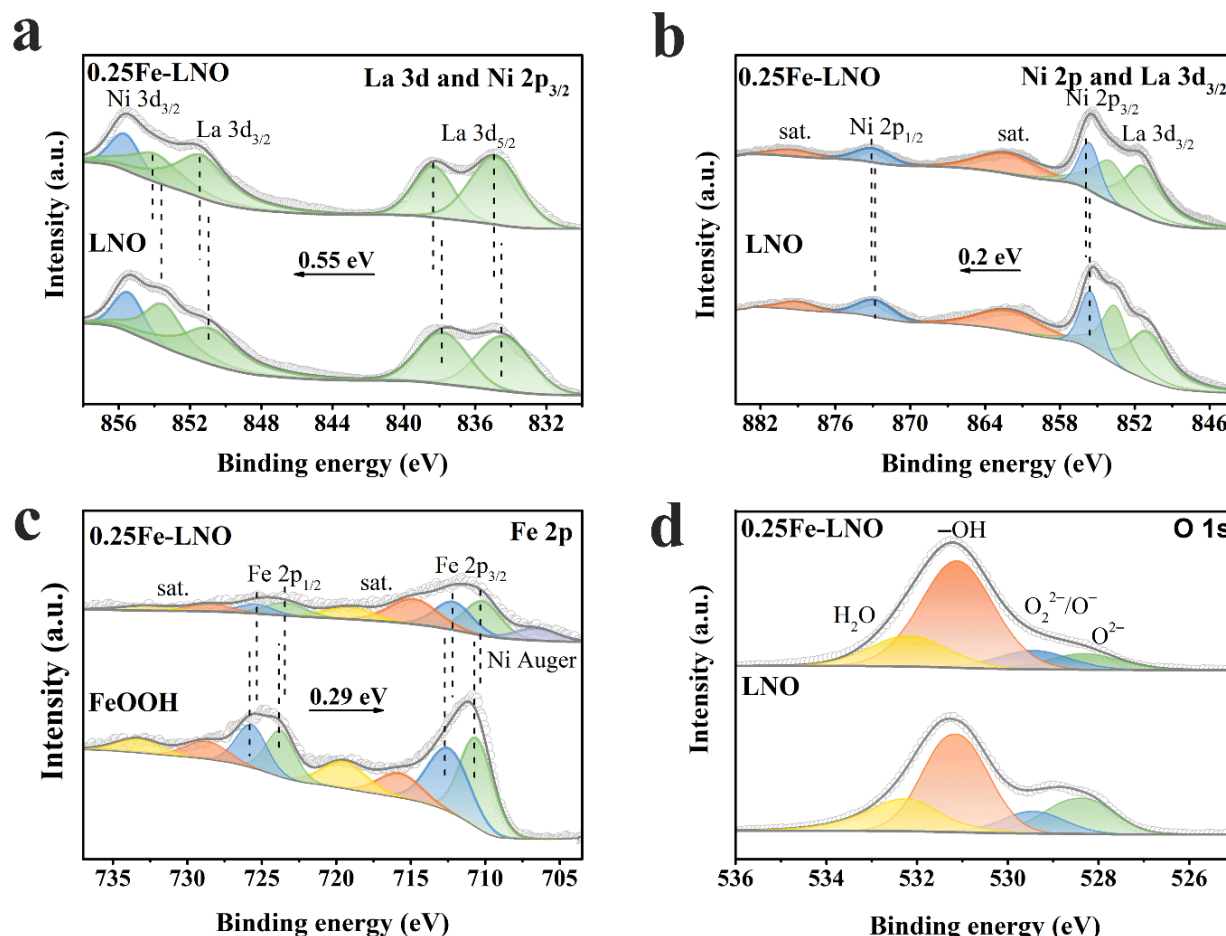


**Figure 3.** XPS spectra of (a) La 3d, (b) Ni 2p, (c) Fe 2p and (d) O 1s.

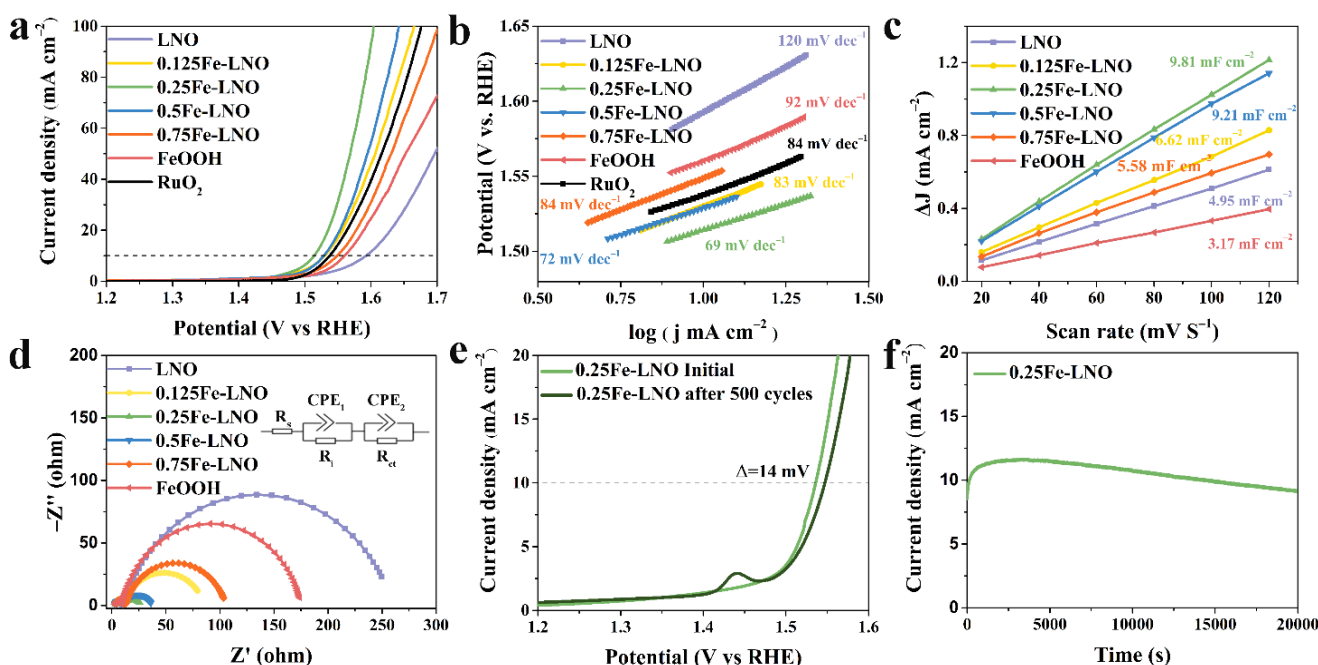


**Figure 4.** (a) LSV of LNO, FeOOH and Fe-LNO samples. (b) The corresponding Tafel plots. (c) Linear fits of half capacitive currents versus scan rates for the extraction of the double-layer capacitances. (d) Nyquist plots. The inset of (d) is the equivalent circuit diagram. (e) The initial polarization curves and the 500th cycles of 0.25Fe-LNO. (f) The chronoamperometric curves of 0.25Fe-LNO.

To further elucidate the enhanced electrochemical performance of 0.25Fe-LNO, cyclic voltammetry (CV) and EIS measurements were carried out. The CV curves measured from  $20 \text{ mV S}^{-1}$  to  $120 \text{ mV S}^{-1}$  of the LNO,  $x\text{Fe-LNO}$  and FeOOH samples are displayed in Figure S9 (Supplementary Materials). The electrochemically active surface area (ECSA) is in direct proportion to the double-layer capacity ( $C_{dl}$ ) [10,55,56]. The  $C_{dl}$  value of the 0.25Fe-LNO ( $9.81 \text{ mF cm}^{-2}$ ) is approximately 3.1 and 2.0 times higher than that of the FeOOH nanosheets ( $3.17 \text{ mF cm}^{-2}$ ) and LNO nanorods ( $4.95 \text{ mF cm}^{-2}$ ), indicating that the composite holds more electrocatalytically active sites than the single component (Figure 4c). The increased ECSA should be the reason, at least in part, for the enhanced OER activity of the 0.25Fe-LNO catalyst, which is highly consistent with the results of SSA discussed above. The LSV curves normalized by the ECSA of LNO,  $x\text{Fe-LNO}$ , FeOOH and RuO<sub>2</sub> are presented to probe the intrinsic activity of the active sites in Figure S10 (Supplementary Materials). Among them, 0.25Fe-LNO has the highest intrinsic activity, indicating that the composite can not only increase the ECSA but also enhance the intrinsic activity. In Figure 4d, the Nyquist plots of each catalyst are manifested as two semi-circles, and the semicircles at the lower and higher frequency ranges represent the interface resistance and charge transfer resistance, respectively [57]. The corresponding equivalent circuit, which consists of the solution resistance ( $R_s$ ), the interface resistance ( $R_i$ ), the charge-transfer resistance ( $R_{ct}$ ) and two constant phase elements (CPE), is shown in the inset of Figure 4d. We found that the  $R_{ct}$  of 0.25Fe-LNO ( $19.1 \Omega$ ) was significantly reduced in comparison with those of LNO ( $250.6 \Omega$ ) and FeOOH ( $166.4 \Omega$ ), suggesting that the composite catalyst possesses rapid charge-transfer kinetics [58,59]. The more fitting parameters of the Nyquist plots are listed in Table S1 (Supplementary Materials), and the trend of  $R_{ct}$  is in line with the results of the Tafel slopes. To demonstrate the positive effect of the close contact between LNO and FeOOH, the electrochemical performance of the LaNiO<sub>3</sub>/FeOOH composite prepared by physical mixing (0.25Fe/LNO) was measured as a comparison (Figure S11, Supplementary Materials). 0.25Fe/LNO displays increased OER activity when compared with LNO and FeOOH. However, the OER performance of 0.25Fe/LNO is far inferior to that of 0.25Fe-LNO due to the smaller active surface area

and the larger charge-transfer resistance. Compared with 0.25Fe/LNO, 0.25Fe-LNO exhibits enhanced synergy and charge transfer between LNO and FeOOH. In addition, the turnover frequency (TOF) of the LNO, xFe-LNO and FeOOH catalysts at 1.60 V vs. RHE was calculated and is listed in Table S2 (Supplementary Materials). 0.25Fe-LNO exhibits a TOF value of  $0.243\text{ S}^{-1}$ , an order of magnitude higher than those of LNO ( $0.031\text{ S}^{-1}$ ) and FeOOH ( $0.022\text{ S}^{-1}$ ), proving that 0.25Fe-LNO possesses superior intrinsic activity [7]. The durability test shows that the overpotential of the 0.25Fe-LNO composite catalyst only increased by 14 mV at the current density of  $10\text{ mA cm}^{-2}$  after 500 CV cycles (Figure 4e). The peak at 1.45 V vs. RHE after 500 CV cycles is the oxidation peak of the Ni species, because the Ni based electrocatalyst  $\text{LaNiO}_3$  experiences the self-surface reconstruction during the electrochemical activation process, forming the amorphous active phase. [53,60]. A clear activation process is also observed during the first as-shown 20,000 s (Figure 4f). For the Chronoamperometry test, the Ni foam was covered by the catalyst as the working electrode, and the interaction and the interface effect between the catalyst and the Ni foam are usually negligible [22,59]. On the one hand, the activity of the Ni foam is far inferior to that of the prepared catalyst (Figure S12, Supplementary Materials); on the other hand, the catalyst dropped on the Ni foam is on a microscale and has less effect than that growing on it.

### 3. Materials and Methods

#### 3.1. Material Synthesis

##### 3.1.1. Synthesis of LNO Nanorods

The LNO nanorods were synthesized by the hydrothermal method. A stoichiometric amount of  $\text{La}(\text{NO}_3)_3 \cdot 6\text{H}_2\text{O}$  (0.125 mmol, 54.2 mg) and  $\text{Ni}(\text{HCO}_2)_2 \cdot 2\text{H}_2\text{O}$  (0.125 mmol, 24.1 mg) were dissolved in 22.5 mL of deionized (DI) water followed by strong stirring to form a clear solution. Then, 2.5 mL 1 M KOH solution was slowly dropped into it to form a light green suspension and was continuously stirred for 15 min. Thereafter, the suspension was transferred into a 50 mL Teflon-lined stainless-steel autoclave and heated at  $180\text{ }^\circ\text{C}$  for 10 h in an oven. The resulting product was washed by DI after cooling to room temperature naturally and then dried. The light green powders were calcined at  $250\text{ }^\circ\text{C}$  for 2 h and then calcined at  $650\text{ }^\circ\text{C}$  for 5 h in air, with the heating rate at  $5\text{ }^\circ\text{C min}^{-1}$ . The obtained black powders were stirred in 12.5 mL 0.01 M  $\text{HNO}_3$  solution for 15 min to remove the impurities. The LNO nanorods were obtained after being dried.

##### 3.1.2. Synthesis of xFe-LNO ( $x = 0.125, 0.25, 0.5, 0.75$ )

Different amounts of the substance  $\text{K}_2\text{FeO}_4$  were dissolved in 50 mL 6 M NaOH solution by sonication for 10 min to obtain the  $\text{K}_2\text{FeO}_4$  solution with different concentrations. The role of NaOH is to regulate the hydrolysis rate of  $\text{K}_2\text{FeO}_4$ , which can promote uniform distribution of the composites. Next, the as-prepared  $\text{LaNiO}_3$  nanorods (0.375 mmol) were added into the solution and sonicated for another 10 min to disperse uniformly. In addition,  $x$  stands for the molar ratios of  $\text{K}_2\text{FeO}_4:(\text{LaNiO}_3 + \text{K}_2\text{FeO}_4)$  in the xFe-LNO samples. For example, the 0.25Fe-LNO sample with the best OER catalytic performance corresponds to 0.125 mmol  $\text{K}_2\text{FeO}_4$ . Subsequently, the above suspension was stirred for 24 h. Finally, the xFe-LNO samples were obtained after being washed several times with DI water.

#### 3.2. Material Characterizations

The phase structures were determined by X-ray diffraction (XRD, D8-Focus with Cu K $\alpha$  radiation, BRUKER, Karlsruhe, Germany). The Raman spectra were scanned with an excitation wavelength of 532 nm on a Horiba LabRAM HR Evolution instrument (HORIBA Scientific, Paris, France). The morphology and microstructure of the samples were characterized by scanning electron microscopy (SEM, S4800, HITACHI, Tokyo, Japan) and transmission electron microscopy (TEM, JEM-F200, JEOL, Tokyo, Japan). The Brunauer–Emmett–Teller (BET) specific surface area of the samples was obtained via  $\text{N}_2$  desorption–adsorption isotherms (SSA-7000, BJ Bulider, Beijing, China). The surface chemical states

were analyzed by X-ray photoelectron spectroscopy (XPS, Thermo Scientific K-Alpha+, ThermoFisher Scientific, Waltham, MA, USA). For XPS, the pass energy is 50.00 eV, and the photoemission angle is 45°. To remove the charging effect leading to the peak positions' shift towards high binding energy, charge compensation was used during the testing, and the energy was calibrated by C 1s = 284.8 eV for all samples.

### 3.3. Electrochemical Measurements

All of the electrochemical measurements were performed in a 1 M KOH electrolyte in a standard three-electrode system on a CHI 760E (Shanghai Chenhua Instrument, Shanghai, China) electrochemical station at room temperature, in which a graphite rod and Ag/AgCl (3.5 M KCl) were respectively applied as the counter and reference electrodes. A glassy carbon (GC) electrode with a diameter of 3 mm, which was covered by a thin catalyst film, was used as the working electrode (except for special instructions). All the catalysts were mixed with conductive carbon (Ketjenblack carbon) at a mass ratio of 7:3 to remove the electrode conductivity limitation. Typically, 3.5 mg of the as-prepared catalyst and 1.5 mg of Ketjenblack carbon were dispersed in a 1 mL solution containing 0.45 mL deionized water, 0.5 mL ethanol and 50  $\mu$ L 0.5 wt% Nafion solution, followed by ultrasonication for at least 1 h to form a homogeneous ink. Then, 5  $\mu$ L of ink was dropped on the GC electrode with a catalyst loading density of 0.352 mg<sub>total</sub> cm<sup>-2</sup> (0.246 mg<sub>cat</sub> cm<sup>-2</sup>) and dried at room temperature. The measured potentials were calibrated to the standard reversible hydrogen electrode (RHE) according to the Nernst equation ( $E_{\text{RHE}} = E_{\text{Ag/AgCl}} + 0.059 \text{ pH} + 0.196$ ).

The linear sweeping voltammograms (LSVs) were obtained at a scan rate of 5 mV s<sup>-1</sup> with iR compensation ( $E_{\text{iR corrected}} = E - IR_s$ , where  $R_s$  is the Ohmic resistance of 1 M KOH and  $i$  is the current). The electrochemical double-layer capacitance ( $C_{\text{dl}}$ ) was calculated by cyclic voltammogram (CV) measurements, with different scan rates of 20, 40, 60, 80, 100 and 120 mV S<sup>-1</sup> in a non-Faradaic current region. Electrochemical impedance spectra (EIS) measurements were recorded at 1.56 V versus the RHE in a frequency range of 10<sup>6</sup>–10<sup>-1</sup> Hz under an AC voltage of 5 mV. The ECSA of a catalyst sample was calculated by the formula:  $\text{ECSA} = C_{\text{dl}}/C_s$ , where  $C_s$  is the specific capacitance and was generally around 0.04 mF cm<sup>-2</sup> in the alkaline solution [61,62]. The turnover frequency (TOF) was calculated by the formula:  $\text{TOF} = (j \times A)/(4 \times F \times n)$ , where  $j$  (A cm<sup>-2</sup>) is the current density obtained by the LSV measurement,  $A$  is the geometric area of the GC with catalysts (0.07065 cm<sup>-2</sup>),  $F$  is the Faraday constant (96485.3 C mol<sup>-1</sup>) and  $n$  is the number of active sites of the catalysts coated on the electrode. The stability test of the 0.25Fe-LNO by CV cycling was conducted in a potential range of 1.0–1.58 V versus the RHE at a scan rate of 100 mV s<sup>-1</sup>, and a chronoamperometry test was conducted at 1.56 V versus the RHE with Ni foam covered by the catalyst (0.375 mg<sub>total</sub> cm<sup>-2</sup>) as the working electrode.

## 4. Conclusions

In summary, we proposed a two-step strategy for the synthesis of perovskite oxides and FeOOH heterostructures with an interesting 1D-2D hierarchical structure. By adjusting the different ratio of the two components, a variety of xFe-LNO composites were prepared. The catalytic performance test shows that the optimized 0.25Fe-LNO catalyst displays a significantly enhanced the OER performance in alkaline electrolytes in comparison to the pristine LaNiO<sub>3</sub> nanorods and FeOOH nanosheets, even outperforming the RuO<sub>2</sub>. We found that the enhanced performance could be explained by the morphology engineering of LNO and the synergistic effect of the perovskite oxides and FeOOH. The introduction of this hierarchical structure not only increases the electrochemically active surface area but also results in an abundant contact area between LNO and FeOOH. Therefore, an accelerated charge transfer and synergistic effect are observed. This strategy also provides a new way to obtain perovskite oxides OER catalysts with better performance.

**Supplementary Materials:** The following supporting information can be downloaded at: <https://www.mdpi.com/article/10.3390/catal12060594/s1>, Figure S1: SEM image of FeOOH nanosheets;

Figure S2: N<sub>2</sub> adsorption–desorption isotherms of LNO and 0.25Fe-LNO; Figure S3: TEM image of 0.25Fe-LNO; Figure S4: HRTEM image of LNO; Figure S5: HAADF-TEM image of 0.25Fe-LNO and the corresponding elemental mapping images; Figure S6: XPS survey spectra of LNO and 0.25Fe-LNO; Figure S7: (a) LSV of LNO, FeOOH, Fe-LNO and IrO<sub>2</sub> samples. (b) The corresponding Tafel plots; Figure S8: (a) LSV of LNO, FeOOH and 0.25Fe-LNO samples without Ketjenblack carbon. (b) The corresponding Tafel plots; Figure S9: CV curves measured from 20 mV S<sup>-1</sup> to 120 mV S<sup>-1</sup> of (a) LNO, (b) 0.125Fe-LNO, (c) 0.25Fe-LNO, (d) 0.5Fe-LNO, (e) 0.75Fe-LNO and (f) FeOOH; Figure S10: ECSA-normalized LSV of LNO, xFe-LNO, FeOOH and RuO<sub>2</sub>; Figure S11: (a) LSV of LNO, FeOOH, 0.25Fe-LNO and 0.25Fe/LNO samples. (b) The corresponding Tafel plots. (c) Linear fits of half capacitive currents versus scan rates for the extraction of the double-layer capacitances. (d) Nyquist plots; Figure S12: The LSV of Ni foam; Table S1: The fitting parameters of Nyquist plots; Table S2: TOF @ 1.60 V vs. RHE (S<sup>-1</sup>) of the LNO, xFe-LNO and FeOOH samples. Table S3: Atomic ratios of xFe-LNO from the SEM-EDS results.

**Author Contributions:** Conceptualization, X.F.; methodology, M.S.; software, M.S.; validation, W.P., Y.L., F.Z., Q.X. and X.F.; formal analysis, M.S.; investigation, M.S.; resources, X.F.; data curation, M.S.; writing—original draft preparation, M.S.; writing—review and editing, Q.Z., Q.C. and X.H.; visualization, M.S.; supervision, X.F., W.P., Y.L., F.Z. and Q.X.; project administration, X.F.; funding acquisition, X.F., W.P., Y.L., F.Z. and Q.X. All authors have read and agreed to the published version of the manuscript.

**Funding:** This research was funded by the National Natural Science Funds of China (grant number 21878226), the Innovative Research Group Project of the National Natural Science Foundation of China (grant number 22121004) and the Haihe Laboratory of Sustainable Chemical Transformations for financial support (grant number CYZC202107).

**Data Availability Statement:** Not applicable.

**Conflicts of Interest:** The authors declare no conflict of interest.

## References

1. Liu, W.; Zheng, D.; Deng, T.; Chen, Q.; Zhu, C.; Pei, C.; Li, H.; Wu, F.; Shi, W.; Yang, S.W.; et al. Boosting Electrocatalytic Activity of 3d-Block Metal (Hydro)oxides by Ligand-Induced Conversion. *Angew. Chem. Int. Edit.* **2021**, *60*, 10614–10619. [[CrossRef](#)] [[PubMed](#)]
2. Wang, H.F.; Tang, C.; Zhang, Q. A Review of Precious-Metal-Free Bifunctional Oxygen Electrocatalysts: Rational Design and Applications in Zn-Air Batteries. *Adv. Funct. Mater.* **2018**, *28*, 1803329. [[CrossRef](#)]
3. Chu, S.; Majumdar, A. Opportunities and challenges for a sustainable energy future. *Nature* **2012**, *488*, 294–303. [[CrossRef](#)]
4. Zhou, J.; Zhang, L.; Huang, Y.C.; Dong, C.L.; Lin, H.J.; Chen, C.T.; Tjeng, L.H.; Hu, Z. Voltage- and time-dependent valence state transition in cobalt oxide catalysts during the oxygen evolution reaction. *Nat. Commun.* **2020**, *11*, 1984. [[CrossRef](#)] [[PubMed](#)]
5. Huang, Z.F.; Song, J.J.; Du, Y.H.; Xi, S.B.; Dou, S.; Nsanzimana, J.M.V.; Wang, C.; Xu, Z.C.J.; Wang, X. Chemical and structural origin of lattice oxygen oxidation in Co-Zn oxyhydroxide oxygen evolution electrocatalysts. *Nat. Energy* **2019**, *4*, 329–338. [[CrossRef](#)]
6. Yu, M.; Budiyanto, E.; Tuysuz, H. Principles of Water Electrolysis and Recent Progress in Cobalt-, Nickel-, and Iron-Based Oxides for the Oxygen Evolution Reaction. *Angew. Chem. Int. Ed. Engl.* **2022**, *61*, e202103824. [[CrossRef](#)]
7. Yao, Y.H.; Zhang, Z.Y.; Jiao, L.F. Development Strategies in Transition Metal Borides for Electrochemical Water Splitting. *Energy Environ. Mater.* **2022**, *5*, 470–485. [[CrossRef](#)]
8. Chen, Q.; Zhang, Q.; Liu, H.; Liang, J.; Peng, W.; Li, Y.; Zhang, F.; Fan, X. Preparation of Hollow Cobalt-Iron Phosphides Nanospheres by Controllable Atom Migration for Enhanced Water Oxidation and Splitting. *Small* **2021**, *17*, e2007858. [[CrossRef](#)]
9. Song, F.; Bai, L.; Moysiadou, A.; Lee, S.; Hu, C.; Liardet, L.; Hu, X. Transition Metal Oxides as Electrocatalysts for the Oxygen Evolution Reaction in Alkaline Solutions: An Application-Inspired Renaissance. *J. Am. Chem. Soc.* **2018**, *140*, 7748–7759. [[CrossRef](#)]
10. Zhai, P.; Zhang, Y.; Wu, Y.; Gao, J.; Zhang, B.; Cao, S.; Zhang, Y.; Li, Z.; Sun, L.; Hou, J. Engineering active sites on hierarchical transition bimetal oxides/sulfides heterostructure array enabling robust overall water splitting. *Nat. Commun.* **2020**, *11*, 5462. [[CrossRef](#)]
11. Yu, J.; Wang, J.; Long, X.; Chen, L.; Cao, Q.; Wang, J.; Qiu, C.; Lim, J.; Yang, S.H. Formation of FeOOH Nanosheets Induces Substitutional Doping of CeO<sub>2-x</sub> with High-Valence Ni for Efficient Water Oxidation. *Adv. Energy. Mater.* **2021**, *11*, 2002731. [[CrossRef](#)]
12. Tang, L.; Chen, Z.; Zuo, F.; Hua, B.; Zhou, H.; Li, M.; Li, J.H.; Sun, Y.F. Enhancing perovskite electrocatalysis through synergistic functionalization of B-site cation for efficient water splitting. *Chem. Eng. J.* **2020**, *401*, 126082. [[CrossRef](#)]

13. Liu, D.; Zhou, P.; Bai, H.; Ai, H.; Du, X.; Chen, M.; Liu, D.; Ip, W.F.; Lo, K.H.; Kwok, C.T.; et al. Development of Perovskite Oxide-Based Electrocatalysts for Oxygen Evolution Reaction. *Small* **2021**, *17*, e2101605. [[CrossRef](#)]
14. Man, I.C.; Su, H.Y.; Calle-Vallejo, F.; Hansen, H.A.; Martínez, J.I.; Inoglu, N.G.; Kitchin, J.; Jaramillo, T.F.; Nørskov, J.K.; Rossmeisl, J. Universality in Oxygen Evolution Electrocatalysis on Oxide Surfaces. *ChemCatChem* **2011**, *3*, 1159–1165. [[CrossRef](#)]
15. Suntivich, J.; May, K.J.; Gasteiger, H.A.; Goodenough, J.B.; Shao-Horn, Y. A perovskite oxide optimized for oxygen evolution catalysis from molecular orbital principles. *Science* **2011**, *334*, 1383–1385. [[CrossRef](#)] [[PubMed](#)]
16. Yan, S.; Xue, Y.; Li, S.; Shao, G.; Liu, Z. Enhanced Bifunctional Catalytic Activity of Manganese Oxide/Perovskite Hierarchical Core-Shell Materials by Adjusting the Interface for Metal-Air Batteries. *ACS Appl. Mater. Inter.* **2019**, *11*, 25870–25881. [[CrossRef](#)] [[PubMed](#)]
17. Zhu, Y.L.; Zhou, W.; Zhong, Y.J.; Bu, Y.F.; Chen, X.Y.; Zhong, Q.; Liu, M.L.; Shao, Z.P. A Perovskite Nanorod as Bifunctional Electrocatalyst for Overall Water Splitting. *Adv. Energy. Mater.* **2017**, *7*, 1602122. [[CrossRef](#)]
18. Zhao, T.W.; Wang, Y.; Chen, X.J.; Li, Y.B.; Su, Z.; Zhao, C. Vertical Growth of Porous Perovskite Nanoarrays on Nickel Foam for Efficient Oxygen Evolution Reaction. *ACS Sustain. Chem. Eng.* **2020**, *8*, 4863–4870. [[CrossRef](#)]
19. He, B.; Tan, K.; Gong, Y.; Wang, R.; Wang, H.; Zhao, L. Coupling amorphous cobalt hydroxide nanoflakes on  $\text{Sr}_2\text{Fe}_{1.5}\text{Mo}_{0.5}\text{O}_{5+\delta}$  perovskite nanofibers to induce bifunctionality for water splitting. *Nanoscale* **2020**, *12*, 9048–9057. [[CrossRef](#)]
20. Zhao, C.; Li, N.; Zhang, R.; Zhu, Z.; Lin, J.; Zhang, K.; Zhao, C. Surface Reconstruction of  $\text{La}_{0.8}\text{Sr}_{0.2}\text{Co}_{0.8}\text{Fe}_{0.2}\text{O}_{3-\delta}$  for Superimposed OER Performance. *ACS Appl. Mater. Inter.* **2019**, *11*, 47858–47867. [[CrossRef](#)]
21. Dai, J.; Zhu, Y.; Zhong, Y.; Miao, J.; Lin, B.; Zhou, W.; Shao, Z. Enabling High and Stable Electrocatalytic Activity of Iron-Based Perovskite Oxides for Water Splitting by Combined Bulk Doping and Morphology Designing. *Adv. Mater. Interfaces* **2018**, *6*, 1801317. [[CrossRef](#)]
22. Chen, G.; Zhu, Y.; Chen, H.M.; Hu, Z.; Hung, S.-F.; Ma, N.; Dai, J.; Lin, H.-J.; Chen, C.-T.; Zhou, W.; et al. An Amorphous Nickel-Iron-Based Electrocatalyst with Unusual Local Structures for Ultrafast Oxygen Evolution Reaction. *Adv. Mater.* **2019**, *31*, e1900883. [[CrossRef](#)] [[PubMed](#)]
23. Sun, J.; Du, L.; Sun, B.; Han, G.; Ma, Y.; Wang, J.; Huo, H.; Du, C.; Yin, G. Bifunctional  $\text{LaMn}_{0.3}\text{Co}_{0.7}\text{O}_3$  Perovskite Oxide Catalyst for Oxygen Reduction and Evolution Reactions: The Optimized  $e_g$  Electronic Structures by Manganese Dopant. *ACS Appl. Mater. Inter.* **2020**, *12*, 24717–24725. [[CrossRef](#)] [[PubMed](#)]
24. Medford, A.J.; Vojvodic, A.; Hummelshøj, J.S.; Voss, J.; Abild-Pedersen, F.; Studt, F.; Bligaard, T.; Nilsson, A.; Nørskov, J.K. From the Sabatier principle to a predictive theory of transition-metal heterogeneous catalysis. *J. Catal.* **2015**, *328*, 36–42. [[CrossRef](#)]
25. Li, Y.X.; Zhang, X.Y.; Wu, Z.J.; Sheng, H.B.; Li, C.; Li, H.Y.; Cao, L.X.; Dong, B.H. Coupling porous Ni doped  $\text{LaFeO}_3$  nanoparticles with amorphous FeOOH nanosheets yields an interfacial electrocatalyst for electrocatalytic oxygen evolution. *J. Mater. Chem. A* **2021**, *9*, 23545–23554. [[CrossRef](#)]
26. Oh, N.K.; Kim, C.; Lee, J.; Kwon, O.; Choi, Y.; Jung, G.Y.; Lim, H.Y.; Kwak, S.K.; Kim, G.; Park, H. In-situ local phase-transitioned  $\text{MoSe}_2$  in  $\text{La}_{0.5}\text{Sr}_{0.5}\text{CoO}_{3-\delta}$  heterostructure and stable overall water electrolysis over 1000 hours. *Nat. Commun.* **2019**, *10*, 1723. [[CrossRef](#)]
27. Gong, C.; Zhao, L.; Li, S.; Wang, H.W.; Gong, Y.S.; Wang, R.; He, B.B. Atomic layered deposition iron oxide on perovskite  $\text{LaNiO}_3$  as an efficient and robust bi-functional catalyst for lithium oxygen batteries. *Electrochim. Acta* **2018**, *281*, 338–347. [[CrossRef](#)]
28. Subbaraman, R.; Tripkovic, D.; Chang, K.C.; Strmcnik, D.; Paulikas, A.P.; Hirunsit, P.; Chan, M.; Greeley, J.; Stamenkovic, V.; Markovic, N.M. Trends in activity for the water electrolyser reactions on 3d M(Ni,Co,Fe,Mn) hydr(oxy)oxide catalysts. *Nat. Mater.* **2012**, *11*, 550–557. [[CrossRef](#)]
29. Zhang, Z.; He, B.; Chen, L.; Wang, H.; Wang, R.; Zhao, L.; Gong, Y. Boosting Overall Water Splitting via FeOOH Nanoflake-Decorated  $\text{PrBa}_{0.5}\text{Sr}_{0.5}\text{Co}_2\text{O}_{5+\delta}$  Nanorods. *ACS Appl. Mater. Inter.* **2018**, *10*, 38032–38041. [[CrossRef](#)]
30. Liu, J.; Qian, G.; Zhang, H.; Chen, J.; Wang, Y.; He, H.; Luo, L.; Yin, S. Amorphous FeOOH coating stabilizes  $\text{WO}_2\text{-Na}_x\text{WO}_3$  for accelerating oxygen evolution reaction. *Chem. Eng. J.* **2021**, *426*, 131253. [[CrossRef](#)]
31. Zhao, J.W.; Li, C.F.; Shi, Z.X.; Guan, J.L.; Li, G.R. Boosting Lattice Oxygen Oxidation of Perovskite to Efficiently Catalyze Oxygen Evolution Reaction by FeOOH Decoration. *Research* **2020**, *2020*, 6961578. [[CrossRef](#)] [[PubMed](#)]
32. Zhang, X.; Liu, Y.; Dong, S.; Ye, Z.; Wei, Y. Low-temperature synthesized nanocomposites with amorphous FeOOH on  $\text{Ti}3\text{C}2\text{Tx}$  for supercapacitors. *J. Alloys Compd.* **2018**, *744*, 507–515. [[CrossRef](#)]
33. Wang, K.; Du, H.; He, S.; Liu, L.; Yang, K.; Sun, J.; Liu, Y.; Du, Z.; Xie, L.; Ai, W.; et al. Kinetically Controlled, Scalable Synthesis of gamma-FeOOH Nanosheet Arrays on Nickel Foam toward Efficient Oxygen Evolution: The Key Role of In-Situ-Generated gamma-NiOOH. *Adv. Mater.* **2021**, *33*, e2005587. [[CrossRef](#)] [[PubMed](#)]
34. Wang, H.; Wang, J.; Pi, Y.; Shao, Q.; Tan, Y.; Huang, X. Double Perovskite  $\text{LaFe}_x\text{Ni}_{1-x}\text{O}_3$  Nanorods Enable Efficient Oxygen Evolution Electrocatalysis. *Angew. Chem. Int. Ed. Engl.* **2019**, *58*, 2316–2320. [[CrossRef](#)] [[PubMed](#)]
35. Zhang, D.; Song, Y.; Du, Z.; Wang, L.; Li, Y.; Goodenough, J.B. Active  $\text{LaNi}_{1-x}\text{Fe}_x\text{O}_3$  bifunctional catalysts for air cathodes in alkaline media. *J. Mater. Chem. A* **2015**, *3*, 9421–9426. [[CrossRef](#)]
36. Li, Z.; Lv, L.; Ao, X.; Li, J.-G.; Sun, H.; An, P.; Xue, X.; Li, Y.; Liu, M.; Wang, C.; et al. An effective method for enhancing oxygen evolution kinetics of  $\text{LaMO}_3$  ( $M = \text{Ni}, \text{Co}, \text{Mn}$ ) perovskite catalysts and its application to a rechargeable zinc-air battery. *Appl. Catal. B Environ.* **2020**, *262*, 118291. [[CrossRef](#)]
37. Nguyen, T.; Montemor, M.F.  $\gamma$ -FeOOH and amorphous Ni-Mn hydroxide on carbon nanofoam paper electrodes for hybrid supercapacitors. *J. Mater. Chem. A* **2018**, *6*, 2612–2624. [[CrossRef](#)]

38. Nieuwoudt, M.K.; Comins, J.D.; Cukrowski, I. The growth of the passive film on iron in 0.05 M NaOH studied in situ by Raman micro-spectroscopy and electrochemical polarisation. Part I: Near-resonance enhancement of the Raman spectra of iron oxide and oxyhydroxide compounds. *J. Raman. Spectrosc.* **2011**, *42*, 1335–1339. [[CrossRef](#)]
39. Chemelewski, W.D.; Lee, H.C.; Lin, J.F.; Bard, A.J.; Mullins, C.B. Amorphous FeOOH oxygen evolution reaction catalyst for photoelectrochemical water splitting. *J. Am. Chem. Soc.* **2014**, *136*, 2843–2850. [[CrossRef](#)]
40. Colomban, P.; Cherifi, S.; Despert, G. Raman identification of corrosion products on automotive galvanized steel sheets. *J. Raman. Spectrosc.* **2008**, *39*, 881–886. [[CrossRef](#)]
41. Wang, J.; Gao, Y.; Ciucci, F. Mechanochemical Coupling of MoS<sub>2</sub> and Perovskites for Hydrogen Generation. *Acs Appl. Energ. Mater.* **2018**, *1*, 6409–6416. [[CrossRef](#)]
42. Thanh, T.D.; Chuong, N.D.; Balamurugan, J.; Van Hien, H.; Kim, N.H.; Lee, J.H. Porous Hollow-Structured LaNiO<sub>3</sub> Stabilized N,S-Codoped Graphene as an Active Electrocatalyst for Oxygen Reduction Reaction. *Small* **2017**, *13*, 1701884. [[CrossRef](#)] [[PubMed](#)]
43. Choi, M.J.; Kim, T.L.; Kim, J.K.; Lee, T.H.; Lee, S.A.; Kim, C.; Hong, K.; Bark, C.W.; Ko, K.T.; Jang, H.W. Enhanced Oxygen Evolution Electrocatalysis in Strained A-Site Cation Deficient LaNiO<sub>3</sub> Perovskite Thin Films. *Nano Lett.* **2020**, *20*, 8040–8045. [[CrossRef](#)]
44. Si, C.H.; Zhang, C.; Sunarso, J.; Zhang, Z.H. Transforming bulk alloys into nanoporous lanthanum-based perovskite oxides with high specific surface areas and enhanced electrocatalytic activities. *J. Mater. Chem. A* **2018**, *6*, 19979–19988. [[CrossRef](#)]
45. Mickevicius, S.; Grebinskij, S.; Bondarenka, V.; Vengalis, B.; Sliuziene, K.; Orlowski, B.A.; Osinniy, V.; Drube, W. Investigation of epitaxial LaNiO<sub>3-x</sub> thin films by high-energy XPS. *J. Alloys Compd.* **2006**, *423*, 107–111. [[CrossRef](#)]
46. Lima, S.M.; Assaf, J.M.; Pena, M.A.; Fierro, J.L.G. Structural features of La<sub>1-x</sub>Ce<sub>x</sub>NiO<sub>3</sub> mixed oxides and performance for the dry reforming of methane. *Appl. Catal. A Gen.* **2006**, *311*, 94–104. [[CrossRef](#)]
47. Biesinger, M.C.; Payne, B.P.; Grosvenor, A.P.; Lau, L.W.M.; Gerson, A.R.; Smart, R.S.C. Resolving surface chemical states in XPS analysis of first row transition metals, oxides and hydroxides: Cr, Mn, Fe, Co and Ni. *Appl. Surf. Sci.* **2011**, *257*, 2717–2730. [[CrossRef](#)]
48. Feng, J.-X.; Xu, H.; Dong, Y.-T.; Ye, S.-H.; Tong, Y.-X.; Li, G.-R. FeOOH/Co/FeOOH Hybrid Nanotube Arrays as High-Performance Electrocatalysts for the Oxygen Evolution Reaction. *Angew. Chem. Int. Ed.* **2016**, *55*, 3694–3698. [[CrossRef](#)]
49. Li, K.L.; Liu, X.Y.; Zheng, T.X.; Jiang, D.B.; Zhou, Z.; Liu, C.Q.; Zhang, X.M.; Zhang, Y.X.; Losic, D. Tuning MnO<sub>2</sub> to FeOOH replicas with bio-template 3D morphology as electrodes for high performance asymmetric supercapacitors. *Chem. Eng. J.* **2019**, *370*, 136–147. [[CrossRef](#)]
50. Feng, J.X.; Ye, S.H.; Xu, H.; Tong, Y.X.; Li, G.R. Design and Synthesis of FeOOH/CeO<sub>2</sub> Heterolayered Nanotube Electrocatalysts for the Oxygen Evolution Reaction. *Adv. Mater.* **2016**, *28*, 4698–4703. [[CrossRef](#)]
51. Pan, Y.; Xu, X.; Zhong, Y.; Ge, L.; Chen, Y.; Veder, J.M.; Guan, D.; O’Hayre, R.; Li, M.; Wang, G.; et al. Direct evidence of boosted oxygen evolution over perovskite by enhanced lattice oxygen participation. *Nat. Commun.* **2020**, *11*, 2002. [[CrossRef](#)] [[PubMed](#)]
52. Jung, K.N.; Jung, J.H.; Im, W.B.; Yoon, S.; Shin, K.H.; Lee, J.W. Doped lanthanum nickelates with a layered perovskite structure as bifunctional cathode catalysts for rechargeable metal-air batteries. *ACS Appl. Mater. Interfaces* **2013**, *5*, 9902–9907. [[CrossRef](#)] [[PubMed](#)]
53. Kwon, J.; Han, H.; Jo, S.; Choi, S.; Chung, K.Y.; Ali, G.; Park, K.; Paik, U.; Song, T. Amorphous Nickel-Iron Borophosphate for a Robust and Efficient Oxygen Evolution Reaction. *Adv. Energy Mater.* **2021**, *11*, 2100624. [[CrossRef](#)]
54. Suen, N.T.; Hung, S.F.; Quan, Q.; Zhang, N.; Xu, Y.J.; Chen, H.M. Electrocatalysis for the oxygen evolution reaction: Recent development and future perspectives. *Chem. Soc. Rev.* **2017**, *46*, 337–365. [[CrossRef](#)]
55. Khodabakhshi, M.; Chen, S.; Ye, T.; Wu, H.; Yang, L.; Zhang, W.; Chang, H. Hierarchical Highly Wrinkled Trimetallic NiFeCu Phosphide Nanosheets on Nanodendrite Ni<sub>3</sub>S<sub>2</sub>/Ni Foam as an Efficient Electrocatalyst for the Oxygen Evolution Reaction. *ACS Appl. Mater. Interfaces* **2020**, *12*, 36268–36276. [[CrossRef](#)]
56. Chang, C.; Zhu, S.; Liu, X.; Chen, Y.; Sun, Y.; Tang, Y.; Wan, P.; Pan, J. One-Step Electrodeposition Synthesis of Bimetal Fe- and Co-Doped NiPi/P for Highly Efficient Overall Water Splitting. *Ind. Eng. Chem. Res.* **2021**, *60*, 2070–2078. [[CrossRef](#)]
57. Wang, X.; Zhang, Y.; Si, H.; Zhang, Q.; Wu, J.; Gao, L.; Wei, X.; Sun, Y.; Liao, Q.; Zhang, Z.; et al. Single-Atom Vacancy Defect to Trigger High-Efficiency Hydrogen Evolution of MoS<sub>2</sub>. *J. Am. Chem. Soc.* **2020**, *142*, 4298–4308. [[CrossRef](#)]
58. Li, Z.; Xue, K.H.; Wang, J.; Li, J.G.; Ao, X.; Sun, H.; Song, X.; Lei, W.; Cao, Y.; Wang, C. Cation and Anion Co-doped Perovskite Nanofibers for Highly Efficient Electrocatalytic Oxygen Evolution. *ACS Appl. Mater. Interfaces* **2020**, *12*, 41259–41268. [[CrossRef](#)]
59. Chen, Q.; Gong, N.; Zhu, T.; Yang, C.; Peng, W.; Li, Y.; Zhang, F.; Fan, X. Surface Phase Engineering Modulated Iron-Nickel Nitrides/Alloy Nanospheres with Tailored d-Band Center for Efficient Oxygen Evolution Reaction. *Small* **2022**, *18*, e2105696. [[CrossRef](#)]
60. Li, Y.; Du, X.; Huang, J.; Wu, C.; Sun, Y.; Zou, G.; Yang, C.; Xiong, J. Recent Progress on Surface Reconstruction of Earth-Abundant Electrocatalysts for Water Oxidation. *Small* **2019**, *15*, 1901980. [[CrossRef](#)]
61. McCrory, C.C.L.; Jung, S.H.; Peters, J.C.; Jaramillo, T.F. Benchmarking Heterogeneous Electrocatalysts for the Oxygen Evolution Reaction. *J. Am. Chem. Soc.* **2013**, *135*, 16977–16987. [[CrossRef](#)] [[PubMed](#)]
62. Morales, D.M.; Risch, M. Seven steps to reliable cyclic voltammetry measurements for the determination of double layer capacitance. *J. Phys. Energy* **2021**, *3*, 034013. [[CrossRef](#)]